nature communications

Article

https://doi.org/10.1038/s41467-026-74136-3

Automated synthesis of InSb quantum dots with improved batch-to-batch reproducibility via kinetically matched co-reduction

Received: 8 February 2026

Accepted: 20 May 2026

Published online: 08 June 2026

Check for updates

Yangning Zhang[1,8], Hyeong Woo Ban[2,8], Pan Xia[1,8], Yang Bai[3], Sile Hu[1], Filip Dinic[1], Chang Liu[4], Yixi Li[3], Ehsan Nikbin[5], Shea Sanvordenker[6], Muhammad Imran[1], Benjamin Rehl[1], Lewei Zeng[1], Sjoerd Hoogland[1], Xiao Qi[7], Brian A. Korgel[6], Emory Chan[7] ✉ & Edward H. Sargent[1,2] ✉

Indium antimonide (InSb) colloidal quantum dots (CQDs) are attractive heavy-metal-free absorbers for infrared photodetection, yet their synthesis remains challenging because precursor reduction overlaps with nucleation and growth, hindering kinetic control and yielding broad size distributions. Here we employ an automated workflow to achieve precise control over InSb CQD synthesis, leading to improved batch-to-batch reproducibility and narrow size distributions without laborious post-synthetic size-selective precipitation. We find that InSb CQD formation proceeds through a kinetically matched precursor co-reduction pathway, which requires an In-rich environment to compensate for the faster reduction of Sb^{3+} precursor. Within this framework, we tune CQD size by modulating precursor conversion kinetics through In/Sb precursor molar ratio and reducing agent availability. This kinetically guided size control tunes the first excitonic absorption peak of CQDs across 1120-1650 nm in the short-wave infrared. Optimized CQDs with 0.825 eV bandgap exhibit a small Stokes shift of 32 meV, which is among the smallest reported for InSb CQDs.

Colloidal quantum dots (CQDs) are versatile building blocks for infrared (IR) photodetectors, offering bandgap tunability, solution processability, and compatibility with flexible substrates and readout circuits.[1–3] These advantages enable emerging applications in telecommunications, medical imaging, autonomous vehicles, and consumer electronics.[4,5] Indium antimonide (InSb) is a heavy-metal-free IR absorber with a small bulk bandgap, high carrier mobility, and a large exciton Bohr radius (≈ 60 nm).[6] InSb CQDs are promising materials for IR photodetection because they combine favorable optoelectronic properties and compatibility with the EU directive on the restriction of the use of certain hazardous substances (RoHS), offering a less toxic alternative to Pb- and Hg-based IR photodetectors.

Size uniformity is critical for achieving high-performance InSb CQD devices,[7,8] as strong quantum confinement in the sub-10 nm size regime makes the CQD bandgap highly sensitive to dispersity in size. Even modest size dispersion can cause pronounced inhomogeneous

[1]Department of Electrical and Computer Engineering, University of Toronto, Toronto, ON, Canada. [2]Department of Chemistry, Northwestern University, Evanston, IL, USA. [3]Acceleration Consortium, University of Toronto, Toronto, ON, Canada. [4]Department of Chemistry, University of Chicago, Chicago, IL, USA. [5]Department of Materials Science and Engineering, University of Toronto, Toronto, ON, Canada. [6]McKetta Department of Chemical Engineering and Texas Materials Institute, The University of Texas at Austin, Austin, TX, USA. [7]The Molecular Foundry, Lawrence Berkeley National Laboratory, Berkeley, CA, USA. [8]These authors contributed equally: Yangning Zhang, Hyeong Woo Ban, Pan Xia. ✉e-mail: emchan@lbl.gov; ted.sargent@utoronto.ca

broadening and obscure excitonic absorption features.[9–11] Size heterogeneity also increases energetic disorder in CQD solids, hindering uniform charge transport.[12]

Synthesizing uniform InSb CQDs remains challenging. Existing InSb CQD synthesis protocols rely on manual hot-injection and heat-up approaches employing In^{3+} and Sb^{3+} precursors in the presence of a reducing agent.[9–11,13,14] At the elevated temperatures required for covalent In–Sb bond formation, precursor reduction overlaps with nucleation and growth, which promotes competing reaction pathways and by-products while yielding CQDs with broad size distributions and poorly resolved excitonic features. Consequently, post-synthetic size-selective precipitation (SSP) is commonly required to isolate narrower size fractions.[9,10,14]

However, the SSP process is labor-intensive, reduces material yield, and the outcome strongly depends on subjective decisions by humans.[15] The post-synthetic optical spectra and size distribution can vary substantially across batches even under nominally identical synthesis conditions. CQDs isolated after multiple cycles of SSP no longer reflect the intrinsic quality of as-synthesized reaction product, which complicates mechanistic interpretation based solely on post-SSP results. Therefore, a synthetic platform capable of directly producing CQDs with well-defined and reproducible spectral features, without post-synthetic SSP, is desired for mechanistic studies.

Automated synthesis platforms offer precise and programmable control over process parameters, enabling more reproducible reaction conditions and rapid exploration of multi-dimensional synthetic spaces.[16,17] These capabilities provide a compelling framework for mechanistic studies and for systematic tuning of CQD size and optical properties.[18–20] No automated outcomes have been reported for InSb CQDs. This is likely due to the high sensitivity of their formation kinetics to subtle variations in reaction conditions, coupled with the widespread reliance on labor-intensive post-synthetic SSP processes.

In this work, we develop an automated synthesis workflow that enables more reproducible, SSP-free production of uniform CQDs and allows systematic mapping of the synthetic parameter space. We investigate the InSb CQD formation pathway, revealing the presence of In^0 and Sb^0 intermediates during precursor to monomer conversion. Using the automated workflow, we identify kinetically matched precursor co-reduction as a key requirement for phase-pure InSb CQD formation, which necessitates an In-rich environment to compensate for the faster reduction of Sb^{3+} precursor. We further show that the precursor conversion kinetics can be modulated through In/Sb precursor molar ratio and reducing agent availability, and employ these parameters to tune the CQD size. Guided by these mechanistic insights we achieve InSb CQDs with first excitonic absorption peak tunable across the short-wave IR from 1120 to 1650 nm. Under optimized conditions, InSb CQDs with 0.825 eV bandgap show a small Stokes shift of 32 meV and a long PL lifetime of 59 ns, reflecting high CQD homogeneity and low defect density.

Results

Formation mechanism of InSb CQDs

To enable systematic exploration of the InSb CQD synthetic space, we first needed a baseline synthesis that features automation-compatible chemistry as well as a large synthetic parameter space. To this end, we modified a protocol that employs $InCl_3$ and $SbCl_3$ precursors in the presence of $ZnBr_2$ additives, with the reaction initiated by the injection of a mild reducing agent, alane *N*,*N*-dimethylethylamine (AlH_3·DMEA).[21] The $ZnBr_2$ additive is believed to decelerate the reduction of the antimony precursor through interactions with the reducing agent. This manual route produces InSb CQDs with a first excitonic absorption peak at ≈1420 nm after multiple cycles of SSP, suggesting substantial room for improving intrinsic size uniformity and reproducibility. Moreover, the fundamental reaction pathway underlying InSb formation remains unclear, particularly whether the In^{3+} precursor participates in the redox process or remains unreduced.

To probe the reaction intermediates experimentally, we performed compositional analysis of aliquots extracted from the reaction mixture at different temperatures (50 °C, 160 °C, and 200 °C). X-ray diffraction (XRD) patterns show diffraction peaks assignable to In^0 at all three temperatures, with only weak In^0 peaks at 50 °C that become much stronger at 160 °C and 200 °C (Supplementary Fig. 1). Although no crystalline Sb-related diffraction peaks are observed by XRD at these temperatures, X-ray photoelectron spectroscopy (XPS) supports the formation of Sb^0-containing species at 50 °C (Supplementary Fig. 1). The Sb^0 intermediate is likely in a disordered or poorly crystalline form, while the coexistence of ligand-coordinated Sb species is also possible. At 160 °C, InSb-related XPS features are detected. Together, these results indicate the presence of In^0 and Sb^0 intermediates at 50 °C, while some of the reduced species have converted to InSb by 160 °C.

Based on these observations, we propose a reaction mechanism in which the co-reduction of $InCl_3$ and $SbCl_3$ precursors generates zero-valent In^0 and Sb^0 species, which combine to form In–Sb bonded species that act as monomers (Fig. 1a). The conversion of precursors into zero-valent species may involve additional elementary steps or transient intermediate states, such as mixed-valent or partially reduced intermediates.[14] As suggested in a few recent reports, the In-Sb bonded species can also exist in different forms, such as In-Sb clusters or Sb-incorporated liquid In^0 intermediates, although in these cases a single source In-Sb precursor was used instead of separate precursors.[11,13] These scenarios are compatible with the overall reaction picture proposed here, and further investigation is encouraged to resolve the detailed intermediate states.

To compare the precursor reduction behavior, we performed single-precursor control experiments in the amine medium and monitored their reduction processes by time-resolved video analysis (Supplementary Fig. 2). We focus here on the relative rate of solution darkening and the characteristic time scale of the transition, rather than the absolute darkness. The normalized darkness signal was plotted as a function of time (Supplementary Fig. 3), showing that the Sb^{3+} precursor undergoes substantially faster reduction than the In^{3+} precursor at equal concentration, with approximately tenfold shorter characteristic time (Supplementary Table 1). Increasing the In^{3+} precursor concentration accelerates its reduction and brings the conversion time scales of the two precursors into closer temporal alignment. We further hypothesize that the degree of kinetic matching between the reduction of In^{3+} and Sb^{3+} precursors determines the temporal overlap of In^0 and Sb^0 intermediates and consequently the effective monomer generation flux.

Comparison between automated and manual synthesis

The reaction mechanism described above suggests that the precursor reduction kinetics are highly sensitive to reaction temperature and precursor environment. In conventional manual synthesis, fluctuations in these parameters are difficult to avoid, often resulting in batch-to-batch variability. In addition, the reliance of manual syntheses on SSP makes it difficult to reveal the intrinsic relationships between synthesis conditions and CQD size.

To overcome these limitations and establish an automated synthetic workflow for mechanistic investigation, we sought to translate InSb CQD synthesis to WANDA, the Workstation for Automated Nanomaterial Discovery and Analysis[16] (Fig. 1b and Supplementary Fig. 4). The automated system enables precise and programmable control over reagent delivery and temperature evolution, while the use of low thermal mass reactors (LTMRs) minimizes spatiotemporal heterogeneity during the reaction. This platform also allows sequential execution of multiple reactions and time-resolved sampling, providing a traceable framework for systematically investigating InSb CQD

https://doi.org/10.1038/s41467-026-74136-3

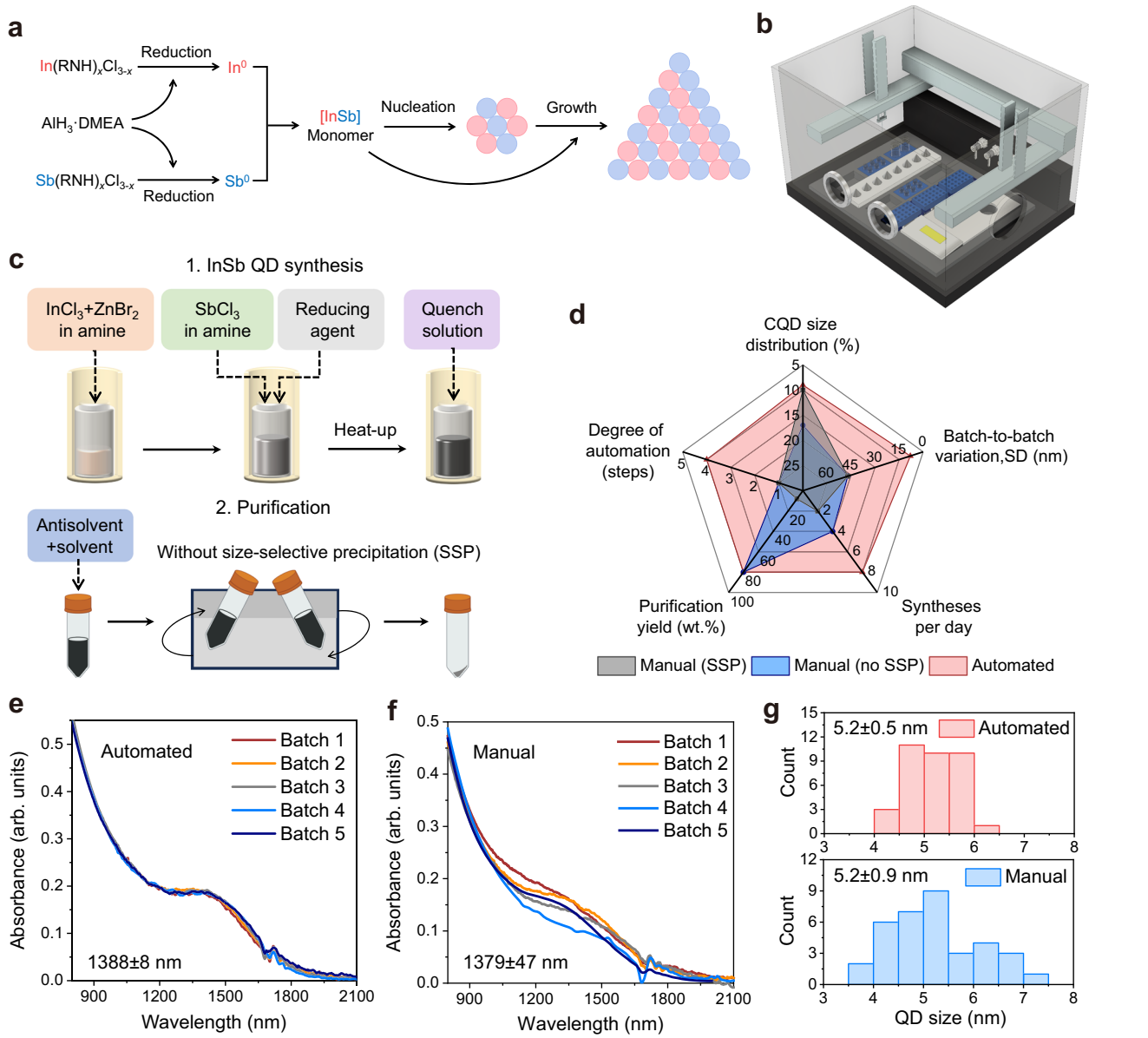

Fig. 1 | Overview of automated InSb CQD synthesis and its advantages. **a** Schematic illustration of the proposed InSb CQD formation mechanism, in which kinetically matched co-reduction of precursors to In^0 and Sb^0 intermediates enables subsequent monomer formation. **b** Schematic illustration of the automated platform for InSb CQD synthesis. **c** Overview of synthesis and purification workflow. **d** Radar chart summarizing the performance of manual synthesis and automated synthesis. The comparison includes CQD size distribution, batch-to-batch variation, number of syntheses per day, purification yield, and degree of automation. Absorption spectra of InSb CQDs synthesized using **e** automated and **f** manual approaches. **g** Size histograms of the corresponding InSb CQDs determined from TEM analysis. The average CQD sizes were 5.20 ± 0.47 nm for automated synthesis and 5.23 ± 0.87 nm for manual synthesis, where values represent mean ± SD from measurements of 35 particles for each sample. In (**d**), the scales are reversed for the CQD size distribution and batch-to-batch variation axes, because lower values indicate improved size uniformity and better reproducibility, respectively. Batch-to-batch variation is quantified as the SD of excitonic absorption peak positions. Source data are provided as a Source Data file.

formation kinetics. Detailed experimental procedures are described in the Methods section.

To reduce post-synthetic processing time and accommodate high-throughput synthesis, we developed a simplified purification procedure that collects the CQDs through a single antisolvent-assisted precipitation step. This SSP-free protocol minimizes material loss due to fractionation, while preserving the intrinsic size distribution generated from synthesis. For quantitative comparison of synthesis outcomes, we used the excitonic absorption peak position and its half width at half maximum (HWHM, see Supplementary Fig. 5 for a graphical explanation) as proxy metrics for CQD size and ensemble inhomogeneity, respectively. The first excitonic peak position of InSb CQDs is highly sensitive to CQD size, while the linewidth of this feature is commonly used in the III-V CQD literature as a practical optical indicator for comparing ensemble inhomogeneity across samples.[22–24]

By establishing an automated synthesis-purification workflow (Fig. 1c), we achieved reproducible synthesis of uniform InSb CQDs on WANDA. A quantitative comparison between automated and manual syntheses is summarized in the radar chart in Fig. 1d, highlighting improved CQD size homogeneity, enhanced batch-to-batch reproducibility, and increased daily throughput enabled by the automated approach (see Supplementary Table 2 for quantitative metrics and the Methods for detailed discussion). The CQDs synthesized across multiple automated batches exhibited highly reproducible optical

https://doi.org/10.1038/s41467-026-74136-3

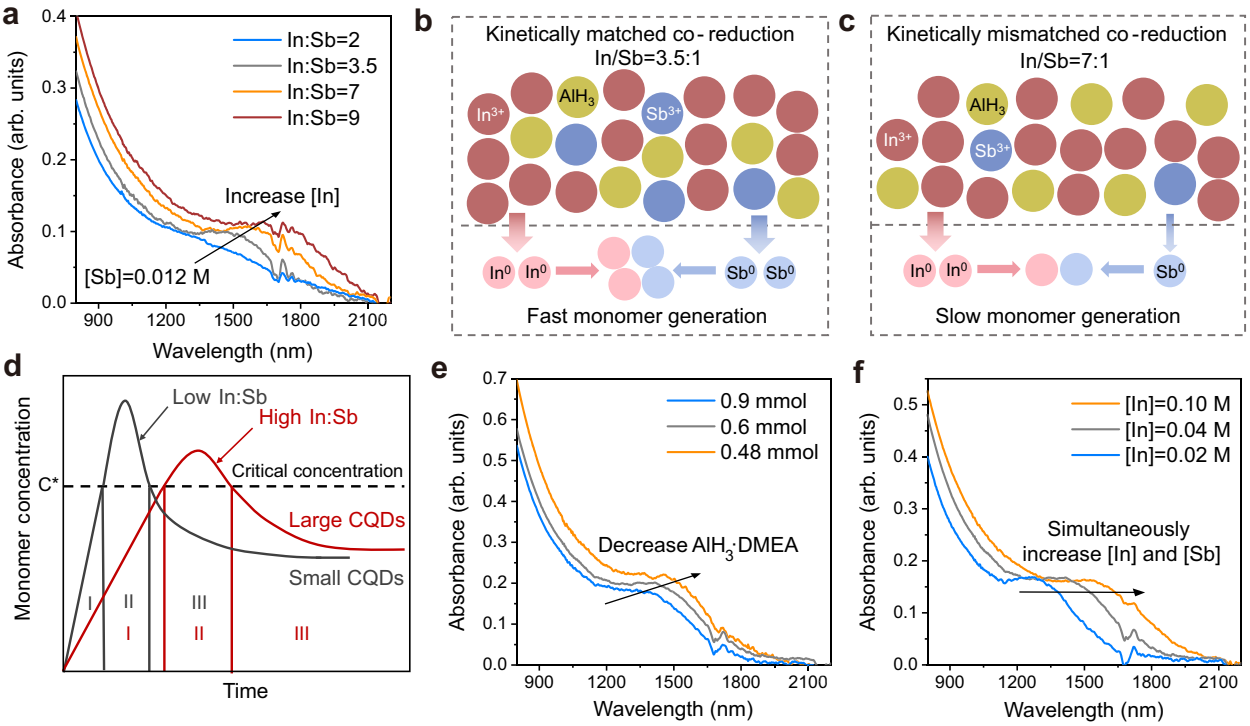

Fig. 2 | Tuning precursor-to-monomer conversion kinetics to control InSb CQD size. a Absorption spectra of InSb CQDs synthesized with different In/Sb precursor molar ratios. Schematic illustration of **b** kinetically matched (In/Sb = 3.5) and **c** kinetically mismatched (In/Sb = 7) precursor co-reduction pathways and their influence on monomer generation. **d** Schematic monomer concentration profiles divided into three regimes: (I) precursor-to-monomer conversion, (II) nucleation, and (III) growth. A low In/Sb ratio (gray curve) leads to small CQDs, whereas a high In/Sb ratio (red curve) leads to large CQDs. Absorption spectra of InSb CQDs synthesized (**e**) with different amounts of AlH_3·DMEA reducing agent and (**f**) with different $InCl_3$ precursor concentrations. For (**a**), the annealing temperature is 260 °C with an annealing time of 60 min, and the [Sb] precursor concentration is 0.012 M. For **e**,**f**, the annealing temperature is 260 °C with an annealing time of 40 min, and the In/Sb molar ratio was maintained at 3.5. Source data are provided as a Source Data file.

properties (Fig. 1e), with a well-defined excitonic absorption peak centered at 1388 ± 8 nm (mean ± standard deviation, SD). In contrast, manually synthesized InSb CQDs showed broad, poorly resolved excitonic features in optical absorption and significant batch-to-batch variations (Fig. 1f), with the absorption peak at 1379 ± 47 nm. The robotically synthesized CQDs exhibited a photoluminescence (PL) peak at 1496 ± 5 nm with an average full width at half maximum (FWHM) of 165 meV, which is 12% narrower than that of manually synthesized counterparts (Supplementary Fig. 6). Transmission electron microscopy (TEM) analysis further corroborates the improved size uniformity of robotically synthesized CQDs (≈9% relative size distribution) and good dispersibility, whereas manually synthesized samples showed a broader size distribution (≈17%) and a substantial fraction of fused particles (Fig. 1g and Supplementary Fig. 7).

Kinetic modulation of precursor reduction and CQD growth

Based on the formation mechanism of InSb CQDs in Fig. 1a, we hypothesized that modulating the precursor stoichiometry would allow us to tune the precursor reduction kinetics, and therefore the product phase purity and CQD size. To test this hypothesis, we varied the In/Sb precursor molar ratio while keeping other conditions the same (annealing at 260 °C for 60 min) and characterized the resulting products (absorption spectra in Fig. 2a and XRD data in Supplementary Fig. 8). At an In/Sb molar ratio of 2:1, the product showed poor dispersibility and no discernible excitonic absorption peak (Fig. 2a). XRD analysis of the precipitate collected during the first centrifugation step reveals a mixed-phase product comprising InSb and metallic Sb (Supplementary Fig. 8). In contrast, increasing the In/Sb precursor molar ratio to 3.5 by adding more $InCl_3$ precursors yielded well-dispersed InSb CQDs without detectable Sb^0 by-products in XRD. Further increasing the In/Sb precursor ratio beyond 3.5 (e.g., to 7 or 9) led to a pronounced redshift in the excitonic absorption peak, from 1465 nm (In/Sb=3.5) to 1565 nm (In/Sb=7) and 1645 nm (In/Sb=9), indicative of increased CQD size. Additionally, metallic In^0 was observed as a by-product at an In/Sb ratio of 7.

We interpret these trends in the context of stoichiometry-tuned matching of precursor reduction kinetics, which determines the temporal overlap of In^0 and Sb^0 intermediates (Fig. 2b, c). Under alane-based reduction conditions, Sb^{3+} is reduced more readily than In^{3+}. The reduction of In^{3+} to In^0 is more demanding and requires a sufficiently high In^{3+} concentration. At low In/Sb molar ratios (e.g., In/Sb=2), a large fraction of AlH_3·DMEA is preferentially consumed during the reduction of Sb^{3+} to Sb^0, whereas the reduction of In^{3+} to In^0 remains sluggish. This temporal mismatch causes Sb^0 to accumulate and crystallize independently, resulting in Sb^0/InSb mixed-phases. Increasing the In/Sb ratio (e.g., In/Sb=3.5, Fig. 2b) accelerates In^0 generation and enables temporal overlap of In^0 and Sb^0, thereby favoring selective formation of InSb CQDs. At higher In/Sb ratios (e.g., In/Sb=7, Fig. 2c), In^0 generation outpaces Sb^0 generation. This kinetic mismatch reduces the monomer generation rate and leads to fewer nucleation events. As a result, the available InSb monomers are distributed among a smaller population of nuclei and are consumed predominantly by growth, yielding larger InSb CQDs (Fig. 2d).

The stoichiometry-based size tuning strategy may extend beyond InSb CQDs to other III-V CQDs. We synthesized InAs CQDs by a modified co-reduction method employing In^{3+} and As^{3+} precursors, as detailed in the Methods.[25] Increasing the In/As precursor molar ratio

https://doi.org/10.1038/s41467-026-74136-3

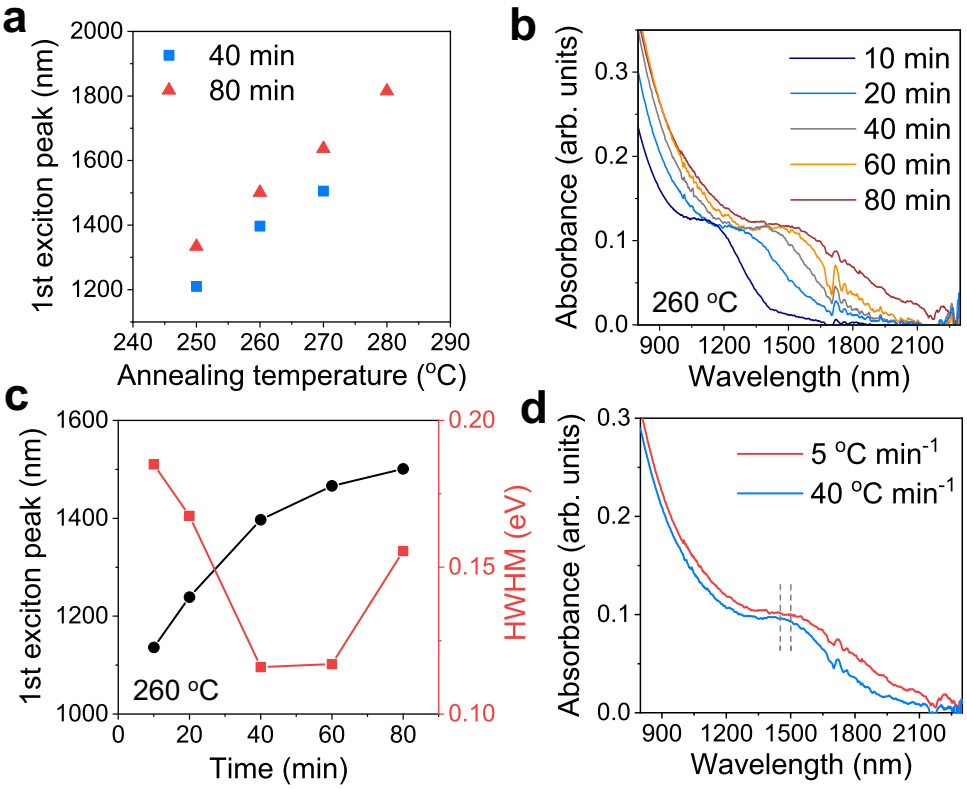

Fig. 3 | Effects of annealing conditions and ramp rate on CQD growth kinetics. **a** Evolution of the first excitonic absorption peak center as a function of annealing temperature (250 °C–280 °C) with a fixed annealing time (40 or 80 min). **b** Absorption spectra of InSb CQDs synthesized at 260 °C annealing temperature for varying durations (10–80 min). **c** Evolution of the first excitonic absorption peak center and the corresponding HWHM as a function of annealing time. **d** Absorption spectra of InSb CQDs synthesized at different ramp rates (5 °C vs. 40 °C min^{-1}). Source data are provided as a Source Data file.

also led to a red-shift of the first excitonic absorption peak (Supplementary Fig. 9), suggesting the formation of larger InAs CQDs.

Beyond precursor stoichiometry, the monomer generation rate can also be modulated by the availability of hydride species, as it directly governs the conversion rate of precursors to zerovalent intermediates. We find that decreasing the amount of AlH_3·DMEA reducing agent leads to the formation of larger CQDs (Fig. 2e), consistent with a reduced population of nuclei under lower effective hydride availability. We note that the active reducing species may not be free AlH_3 alone, but may also include amine-coordinated aluminum hydride species.[14] In addition, Zn halide additives can form adducts with AlH_3·DMEA, thereby slowing the release of hydride species.[14] We find that increasing the concentration of Zn (at fixed In concentration and fixed In/Sb molar ratio) caused a redshift in the excitonic peak (Supplementary Fig. 10), indicating larger average CQD sizes.

Furthermore, the overall precursor concentration also modulates the CQD size. Under a fixed amount of AlH_3·DMEA, increasing the concentration of both $InCl_3$ and $SbCl_3$ precursors while maintaining a constant In/Sb ratio of 3.5 leads to a systematic redshift in the excitonic peak (Fig. 2f), suggesting the formation of larger CQDs. Dilution of the reaction mixture further modulates CQD size: dilution with coordinating oleylamine (OLAM) leads to smaller CQDs, while non-coordinating heptadecane yields larger CQDs (Supplementary Fig. 11).

In many classical CQD systems, such as CdSe and InP,[26,27] increasing precursor concentration typically leads to higher monomer supersaturation, which promotes burst nucleation and results in a larger nuclei population and consequently smaller average CQD size. However, InSb CQDs studied here deviate from this trend, because InSb formation proceeds through a co-reduction pathway. Under a fixed hydride supply, increasing the overall precursor concentration does not increase the instantaneous generation rate of In^0 and Sb^0 intermediates. Instead, these intermediates are produced gradually over an extended time window, keeping the monomer concentration below the threshold needed for additional nucleation. The monomers generated at later stages feed the growth of existing nuclei, therefore yielding larger InSb CQDs.

To elucidate the growth kinetics of InSb CQDs, we then investigated the impact of annealing temperature and time on CQD size evolution. At a fixed annealing time, increasing the annealing temperature from 250 °C to 280 °C resulted in a progressive redshift of the first excitonic absorption peak (Fig. 3a), reflecting promoted CQD growth at elevated temperatures. However, higher annealing temperatures also result in broadened absorption features (Supplementary Fig. 12), indicating degraded size uniformity. This behavior is likely due to ligand desorption and particle coalescence at higher temperatures. Automatic sampling at a fixed annealing temperature of 260 °C enables us to track CQD growth over time, showing a time-dependent redshift of the first absorption peak (Fig. 3b). The absorption peak HWHM (Fig. 3c) is large at initial annealing stage (10 min) and gradually decreases to a minimum between 40 and 60 min. Beyond 60 min, the increase in HWHM indicates broadening of the size distribution, indicative of the onset of Ostwald ripening.

We also studied the influence of ramp rate on CQD size. In our baseline protocol, the slow ramp rate (5 °C min^{-1}) from the precursor injection temperature (50 °C) to the annealing temperature likely allows nucleation to overlap with early-stage growth, which could contribute to CQD size broadening. We hypothesize that accelerating the temperature ramp would compress nucleation within a narrow time window, and facilitate temporal decoupling of nucleation and growth. To test this hypothesis, we changed the ramp rate while keeping annealing temperature (260 °C) and duration (80 min) constant (see Supplementary Fig. 13 for the temperature profile).

https://doi.org/10.1038/s41467-026-74136-3

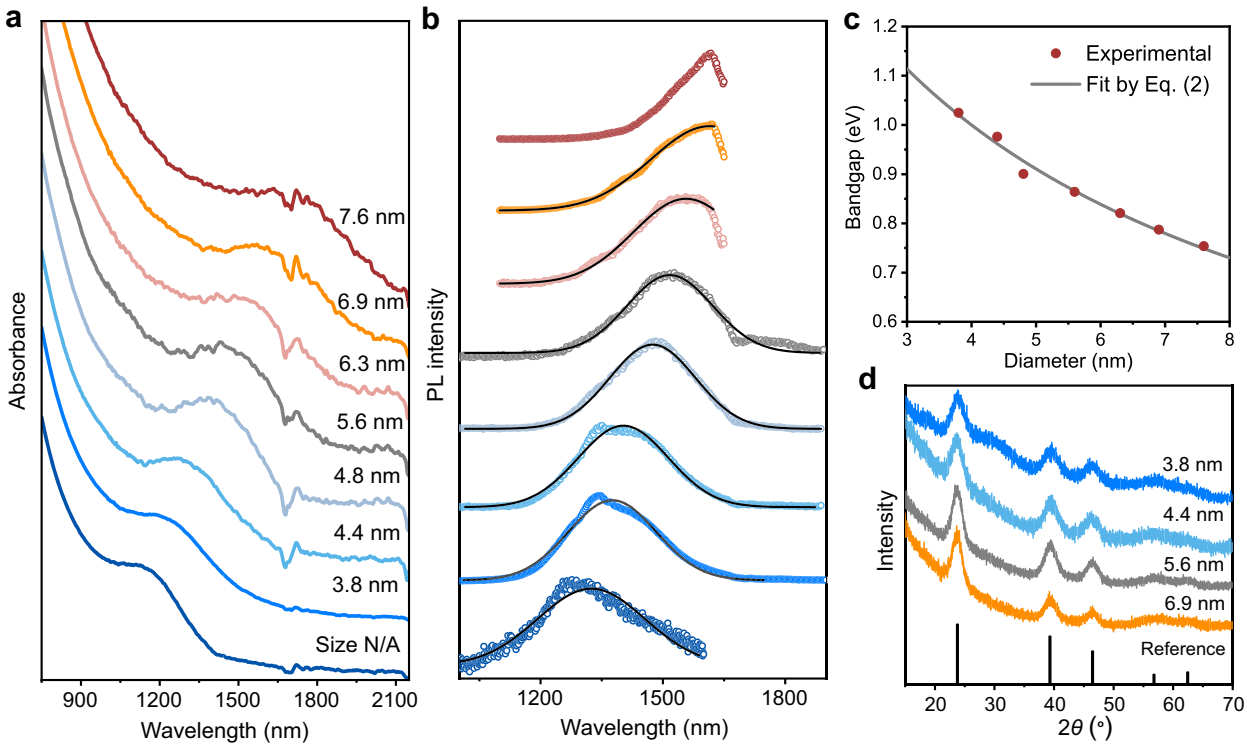

Fig. 4 | Size-dependent optical tunability of InSb CQDs. a Absorption and **b** PL spectra of InSb CQDs with an average size ranging from 3.8 nm to 7.6 nm. **c** Size dependence of the optical bandgap of InSb CQDs. Symbols represent the experimental data, and the solid line shows the fit based on the model given in Eq. (2). **d** XRD patterns of different-sized InSb CQDs and reference zinc-blende InSb (PDF # 06-0208). In (**a**), the dip at around 1700 nm originates from solvent xylene absorption. N/A indicates that the mean size was not available because the CQDs aggregated during additional precipitation for TEM sample preparation. In (**b**), the shoulder-like feature at around 1380 nm in the PL spectra is also due to xylene absorption. Source data are provided as a Source Data file.

Increasing the ramp rate from 5 °C to 40 °C min^{-1} results in a blueshift in the excitonic peak with a reduced HWHM (Fig. 3d), consistent with the formation of smaller and more uniform CQDs observed by TEM (Supplementary Fig. 13). These results suggest that ramp rate primarily affects CQD size uniformity by reducing temporal overlap of nucleation and growth and minimizing the pre-annealing growth.

Spectral tunability and materials characterization

Building upon these mechanistic insights, we achieved spectral tunability across the short-wave infrared region, with the first excitonic absorption peaks spanning from 1120 to 1650 nm, and the corresponding PL peaks ranging from 1325 nm to beyond 1700 nm (Fig. 4a, b). The corresponding CQD sizes were determined from TEM analysis (Fig. 5), and the detailed synthesis conditions are provided in Supplementary Table 3. The optical bandgap extracted from the first excitonic absorption peak decreases gradually with increasing CQD size, from 1.0 eV for 3.8 nm CQDs to 0.75 eV for 7.6 nm CQDs (Fig. 4c). The size-dependent bandgap was fitted using the tight-binding model developed by Allan and Delerue,[28] which has been shown to better describe InSb CQDs than the simple effective-mass approximation.[13,29]

$$E_g(d) = E_g(\infty) + \frac{1}{Ad^2 + Bd + C} \quad (1)$$

where $E_g(\infty)$=0.17 eV for bulk InSb, and d is the CQD diameter (nm). The fitting yields a negligible A term, with $B = 0.1452\ nm^{-1}\ eV^{-1}$ and $C = 0.6241\ eV^{-1}$. Therefore, the expression can be simplified to:

$$E_g(d) = 0.17 eV + \frac{1}{0.1452\ nm^{-1}\ eV^{-1}\ d + 0.6241\ eV^{-1}} \quad (2)$$

This result suggests that over the size range studied here, the bandgap of InSb CQDs primarily follows a $1/d$ dependence, consistent with refs. 13,29.

XRD patterns (Fig. 4d) of the representative samples exhibit the characteristic diffraction peaks of zinc-blende InSb.[30] The TEM images in Fig. 5a–f show that the average size of InSb CQDs can be tuned from 3.8 to 7.6 nm by adjusting the synthetic parameters. To further validate the particle size analysis, we performed small-angle X-ray scattering (SAXS) measurements on representative samples and extracted the effective particle size and dispersity in size. The fitted particle diameters are in good agreement with the TEM results, although the dispersity in size estimated from SAXS is slightly larger than that obtained from TEM (Supplementary Fig. 14 and Supplementary Table 4). The SAXS results also support the use of absorption HWHM as a proxy indicator of size dispersity for CQDs with similar average size: samples with broader absorption HWHM show larger size polydispersity in SAXS (Supplementary Fig. 15).

The larger-sized CQDs adopt a tetrahedral shape, whose 2D projections in TEM vary from triangles to tetragons depending on their orientations with respect to the electron beam.[31] High-angle annular dark-field scanning transmission electron microscopy (HAADF-STEM) images of CQDs further support the tetrahedral shape (Fig. 5g, Supplementary Fig. 16). An enlarged view of an individual CQD (Fig. 5h) reveals clear atomic lattice fringes, and the corresponding fast Fourier transform (FFT, Fig. 5i) pattern matches the [001] zone axis of zinc-blende InSb. The observed particle geometry is consistent with tetrahedral CQDs terminated by {111} facets, except that the vertices of the imaged CQD are not as sharp as those modeled in Fig. 5j. Elemental mapping (Supplementary Fig. 17) reveals uniform distributions of In and Sb throughout the CQDs, indicating compositional homogeneity.

https://doi.org/10.1038/s41467-026-74136-3

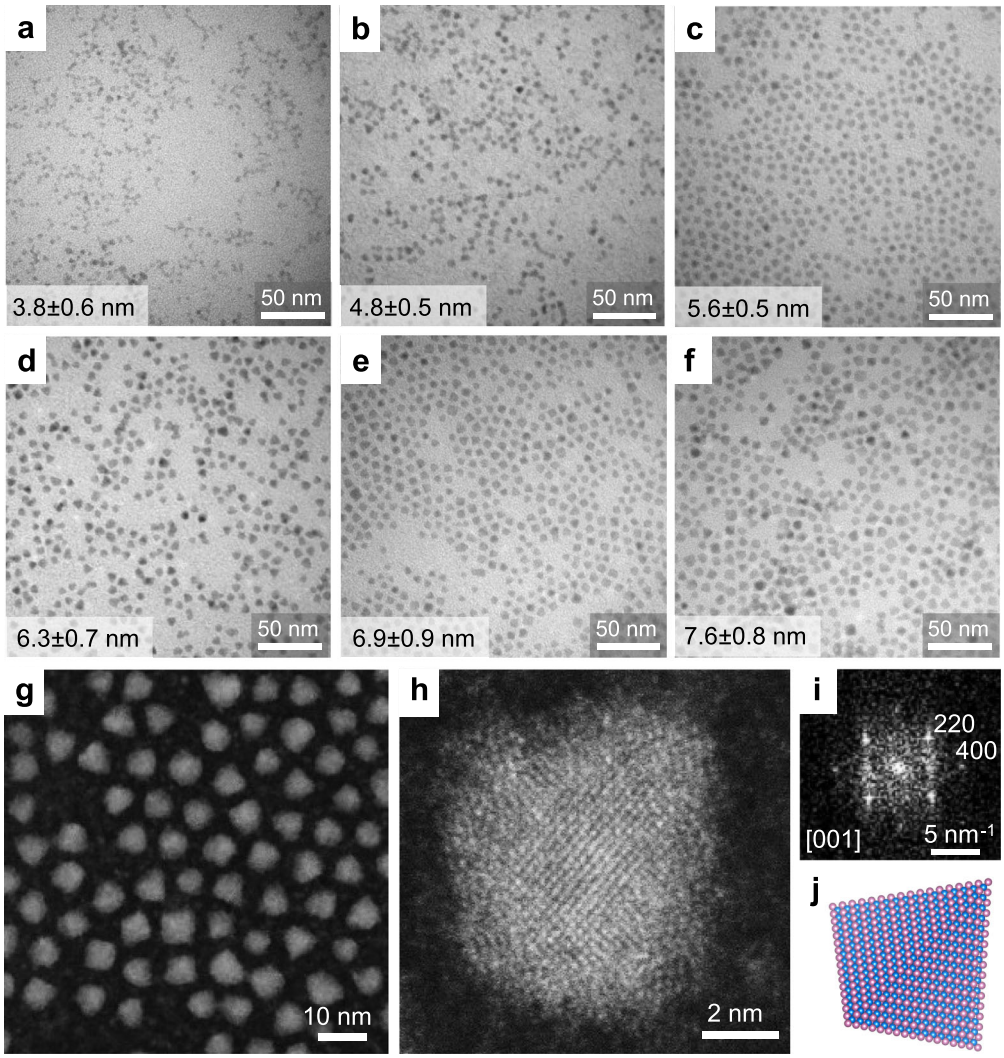

Fig. 5 | Structural characterization of size-tuned InSb CQDs. a–f TEM images of InSb CQDs with average size of 3.8, 4.8, 5.6, 6.3, 6.9, and 7.6 nm, respectively. Values represent mean ± SD from measurements of at least 35 particles for each sample. **g** HAADF-STEM image of the 6.9 nm InSb CQDs. **h** Enlarged high-resolution view of an individual CQD and its corresponding **i** FFT pattern, matching the zinc-blende structure. **j** Schematic illustration of a tetrahedral-shaped CQD terminated by {111} facets. In (**a**–**g**), similar results were obtained from 2 independently prepared samples. In (**i**), the spots in FFT pattern are indexed to the {220} and {400} planes when viewed along the [001] zone axis. In (**j**), the pink and blue atoms represent In and Sb, respectively.

Previous experimental studies on InSb CQDs have predominantly reported quasi-spherical or irregular shapes with limited control over exposed crystal facets.[9–11,13] Theoretical studies suggested that amine and halide co-passivation stabilizes In-terminating {111} facets of tetrahedrally-shaped InAs CQDs.[32] Given that our tetrahedrally-shaped InSb CQDs were synthesized under high $InCl_3$ precursor concentrations (Supplementary Table 3), we believe the combination of a highly In-rich precursor environment and the amine/halide ligand coordination enables facet-selective growth of InSb CQDs by stabilizing In-terminated {111} facets.

To investigate how different kinetic routes influence the optical properties at a fixed CQD size, we focused on a target excitonic absorption wavelength of ≈1500 nm (i.e., bandgap of 0.825 eV), which lies near the technologically important 1550 nm telecommunications band. We selected three representative routes that can reach this target wavelength while preserving reasonable CQD yield and well-resolved excitonic features: (1) moderate-temperature (260 °C) growth with extended annealing (control), (2) low-temperature (250 °C) growth under a highly In-rich precursor environment (target 1), and (3) increased overall precursor concentrations at moderate temperature (target 2). The corresponding synthetic parameters are summarized in the radar chart in Fig. 6a. The high-temperature (≥270 °C) growth route is excluded from this comparison, because it reduces the CQD yield and significantly broadens the absorption linewidth.

The absorption and PL spectra of CQDs obtained from these three routes are compared in Fig. 6b, c. While all three routes produced the first excitonic absorption peaks centered at 0.825 eV, the absorption peak HWHM of targets 1 and 2 were 25% and 12% smaller, respectively, than that of the control (Fig. 6d), indicating improved size homogeneity. Targets 1 and 2 also exhibit nearly identical Stokes shifts (32 meV), which are reduced by half compared to the control and among the smallest Stokes shifts reported for InSb CQDs.[21] After minimizing the influence of external factors during measurement and data analysis, the reduced Stokes shift may be associated with improved size homogeneity and reduced defect density.

To further compare the carrier recombination dynamics among the samples, we performed time-resolved PL measurements (Fig. 6e). The PL decay curves were fitted with a biexponential decay model, yielding a fast decay component (7–12 ns), and a slower component

https://doi.org/10.1038/s41467-026-74136-3

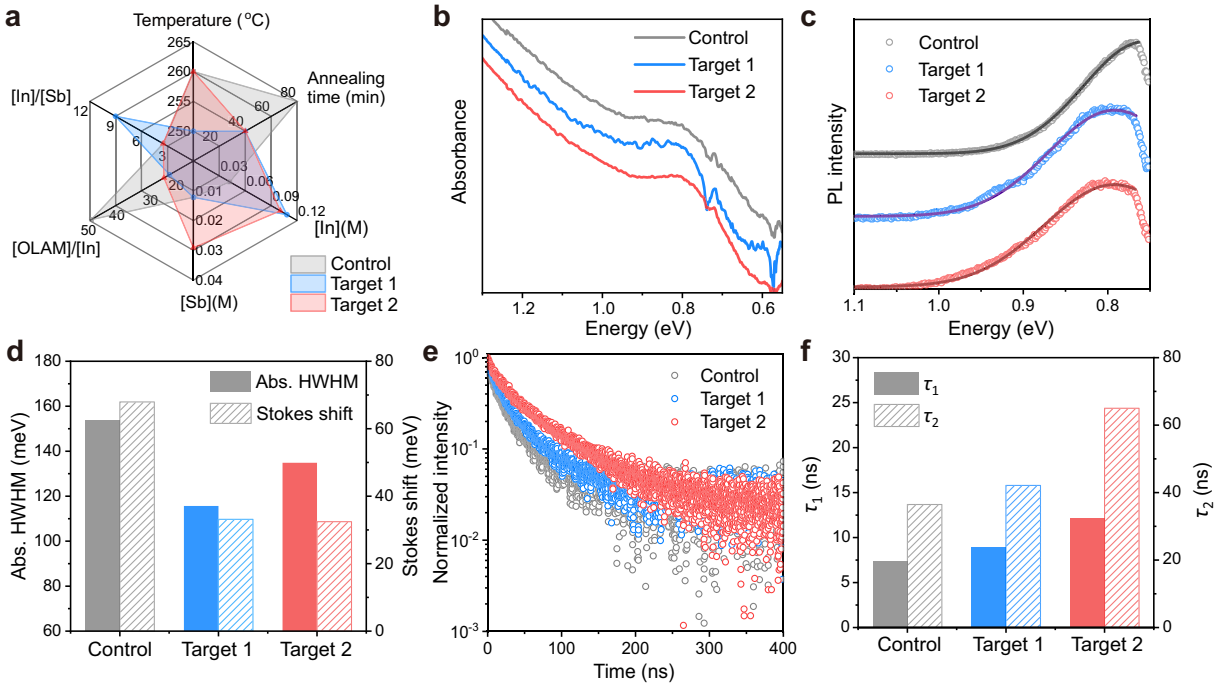

Fig. 6 | Optimization of InSb CQDs with 0.825 eV bandgap through kinetically distinct synthetic routes. a Radar chart visualization of synthesis parameters for three synthetic routes to CQDs with 0.825 eV bandgap, labeled as control, target 1, and target 2. [In] and [Sb] denote the initial concentrations of In^{3+} and Sb^{3+} precursors, respectively. The other synthetic parameters not listed here are kept constant (i.e., 5 °C min^{-1} ramp rate, 0.6 mmol of reducing agent, and 1.28 mmol of $ZnBr_2$). **b**–**f** Optical characterization of the three samples: **b** absorption spectra, **c** PL spectra, **d** summary of absorption peak HWHM and Stokes shift, **e** time-resolved PL decay, and **f** comparison of PL decay components obtained from biexponential decay fitting. In (**c**), the shoulder-like features at around 0.9 eV are attributed to solvent absorption. Source data are provided as a Source Data file.

(36-65 ns), as summarized in Fig. 6f and Supplementary Table 5. According to prior reports on InSb CQDs, the fast component τ_1 is often attributed to non-radiative recombination, while the slower component τ_2 is associated with radiative recombination.[14,29] Relative to the control sample, both targets 1 and 2 show longer τ_1, τ_2, and average lifetime. From target 1 to target 2, τ_1 increases from 8.9 to 12.1 ns, and τ_2 increases from 42.1 to 65.0 ns. Meanwhile, the relative amplitude of the slower component increases from 0.48 to 0.57, accompanied by an increase in the average lifetime from 36.8 to 59.2 ns. Since the CQD sizes are comparable, these changes are unlikely to arise from size effects. Instead, they suggest that the synthetic route for target 2 leads to reduced trap-assisted recombination and a greater contribution from band-edge emission.

XPS analysis provides additional evidence for differences in surface chemistry among the samples. The In/Sb atomic ratios in the CQDs (Supplementary Table 6) determined from XPS decrease from 1.48 (control) to 1.42 (target 1) and 1.34 (target 2), indicating that the CQD surfaces become less In-rich. Excess In, especially undercoordinated In atoms at the CQD surface, can introduce in-gap states that promote non-radiative recombination.[33,34] In addition, target 2 exhibits reduced surface oxidation compared with target 1 and the control (Supplementary Fig. 18). The synthesis of target 2 employed higher $InCl_3$ and $SbCl_3$ precursor concentrations, which may have helped suppress oxidation during synthesis. Density functional theory calculations have shown that oxidation of InSb(111) facets induces local structural distortions and creates trap states within the bandgap.[34] Taken together, the TRPL and XPS results suggest that target 2 has a lower density of defect states than the other samples, consistent with the observed smaller Stokes shift.

We performed solution-phase thiol ligand exchange on target 2 CQDs using our previously reported method,[35] and fabricated field-effect transistor (FET) devices. The exchanged CQD films exhibit p-type transport behavior (Supplementary Fig. 19), and the hole mobility was estimated to be 4×10^{-5} cm^2 V^{-1} s^{-1}. Details of FET device fabrication, measurement, and mobility calculation are provided in the Methods. These preliminary results demonstrate that the CQDs produced by the automated synthesis are compatible with downstream processing needed to form electrically active CQD solids. This highlights the technological relevance of the automated workflow as a promising route toward high-throughput production of infrared CQDs for optoelectronic applications.

Discussion

In summary, we developed a robotic workflow for synthesizing high-quality InSb CQDs with tunable absorption peaks in the range of 1120–1650 nm, eliminating the need for labor-intensive size-selective precipitation. Compared to manual synthesis, the automated method reduced CQD size dispersion by 50% and improved batch-to-batch reproducibility by sixfold, underscoring the importance of precise spatiotemporal control over reaction parameters in this kinetically sensitive system. Our results support a kinetically matched precursor co-reduction pathway for InSb CQD formation, in which temporally overlapping In^0 and Sb^0 intermediates promote monomer generation. We further show that slowing the precursor-to-monomer conversion—by increasing the In/Sb precursor molar ratio, limiting reducing agent availability, or increasing the overall precursor concentration—suppresses nucleation and results in larger-sized CQDs. Structural analysis showed that the increased size is accompanied by a transition toward tetrahedral-shaped CQDs terminated by {111} facets. Under high precursor concentration, CQDs with 0.825 eV bandgap exhibit a small Stokes shift of 32 meV and an average PL lifetime of 59 ns, consistent with improved homogeneity and reduced defect density. More

broadly, these findings establish a kinetically-guided framework for redox-driven InSb CQD synthesis that can be extended to other III-V CQD systems. They also inform future efforts toward programmable and scalable production of III-V CQDs, data-driven optimization, and the integration of automated workflows with downstream processing for optoelectronic device applications.

Methods

Materials

Indium(III) chloride (≥99.999% In) and antimony (III) chloride (≥99.999% Sb) were purchased from Strem Chemicals. Zinc bromide (≥99.999% trace metals basis), zinc chloride (≥99.995% trace metals basis), alane *N*,*N*-dimethylethylamine complex solution (0.5 M in toluene), oleylamine (OLAM, ≥98% primary amine), oleic acid (OA, 90% technical grade), trioctylamine (98%), 2-mercaptoethanol (≥99.0%), acetonitrile (anhydrous, 99.8%), m-xylene (anhydrous, 99.8%), toluene (anhydrous, ≥99%), and ethyl alcohol (pure ≥99.5%, anhydrous) were purchased from Sigma Aldrich. Tris(dimethylamino)arsine (≥99.999%) was purchased from Dock Chemicals. All chemicals were used as received except for OLAM and OA, which were degassed before use.

Preparation of stock solutions

$InCl_3/ZnBr_2$ stock solution was prepared by dissolving 176 mg of $InCl_3$ and 720 mg of $ZnBr_2$ in a mixture of 12 mL OLAM and 3 mL trioctylamine at 70 °C overnight. $SbCl_3$ stock solution was prepared by dissolving 570 mg of $SbCl_3$ in 10 mL OLAM at 70 °C overnight. The quench solution was prepared by mixing 70 mL xylene with 16 mL OA at room temperature. All the processes were conducted inside a nitrogen-filled glovebox.

Synthesis of InSb CQDs

InSb CQDs were synthesized by adapting a previously reported manual protocol[21] to an automated workflow on WANDA.[16] Prior to automated syntheses, the stock solutions were each loaded into the designated deck positions (see Supplementary Fig. 4). For each reaction, a designated amount of preheated $InCl_3/ZnBr_2$ stock solution was dispensed into a 40 mL reaction vial, which was then placed into an LTMR. Reaction parameters, including reagent volumes, temperature ramp rate, annealing temperature, and annealing time, were predefined and executed through an automated reaction library in Symyx Library Studio software. The automated program runs in serial, and each program starts by setting the reactor temperature to 50 °C with stirring. A designated amount of pre-heated $SbCl_3$ stock solution was dispensed into the reactor, followed by the injection of reducing agent (alane *N*,*N*-dimethylethylamine complex solution, 0.6 mmol under baseline conditions). After the injection of each reagent, the dispensing needle was rinsed thoroughly with xylene. After a stabilization period of 5 min, the reaction temperature was increased from 50 °C to the annealing temperature (250 °C–280 °C) at a ramp rate of 5 °C min^{-1}. During the annealing period, aliquots were extracted from the reactions for time-resolved analysis. After completing the annealing step, the reaction vials were cooled rapidly by nitrogen flow through the LTMR cooling shrouds. The reaction was further quenched by the injection of a xylene/OA mixture directly into the vials. All the synthesis and purification processes were conducted inside a nitrogen-filled glovebox whose oxygen level was kept below 15 ppm and water level below 0.1 ppm.

Purification of InSb CQDs

The reaction mixture was transferred into centrifuge tubes and centrifuged at 4427× *g* for 5 min to remove insoluble by-products. The supernatant was collected, to which acetonitrile and xylene were added (typically the volume ratio of reaction product: acetonitrile: xylene is 3:2:1). After centrifuging this mixture, the supernatant should have almost no color, suggesting that most of the quantum dots were precipitated. The purified quantum dots were dispersed in xylene.

Comparison of workflow performance metrics

We compared three workflows using several key performance metrics: automated synthesis, manual synthesis without SSP, and manual synthesis with SSP. The values are summarized in Supplementary Table 2 and the detailed definitions, assumptions, and estimation procedures are described below.

CQD size distribution: The average sizes of CQDs obtained from automated and manual synthesis (no SSP) workflows were 5.20 ± 0.47 nm and 5.23 ± 0.87 nm, corresponding to size distributions of 9% and 17%, respectively. These values were determined from TEM analysis in Supplementary Fig. 7, and the corresponding size histograms in Fig. 1g. For CQDs obtained from manual synthesis followed by post-synthetic SSP, the size distribution is 10% according to ref. 35.

Reproducibility: Batch-to-batch reproducibility was assessed from the variation in excitonic absorption peak positions across five independent batches, quantified as the SD. Lower SD values indicate better batch-to-batch reproducibility. For automated synthesis, the average excitonic absorption peak position is at 1388 ± 8 nm, corresponding to an SD of 8 nm. Manual synthesis without SSP results in 1379 ± 47 nm, corresponding to an SD of 47 nm. For manual synthesis with SSP, batch-to-batch reproducibility was not experimentally determined in this study. We therefore use an estimated SD of 47 nm as an approximation, assuming that SSP does not improve the intrinsic reproducibility of the synthesis.

Syntheses per day: To enable a consistent comparison of number of syntheses per day, we make the following assumptions: (i) reactions are conducted sequentially, rather than in parallel; (ii) time associated with precursor preparation, reactor setup, and post-synthetic characterization is excluded; (iii) the daily operation time is 8 h for manual synthesis and 24 h for automated synthesis. Considering a typical synthetic batch (5 °C min^{-1} ramp rate, 260 °C annealing temperature, 40 min annealing time), the reaction itself requires ≈100 min. Post-synthetic processing adds ≈15 min with the simplified purification protocol, whereas SSP requires ≈75 min for five purification cycles. Each purification cycle includes centrifugation at 4427× *g* for 5 min, followed by isolation of the desired fraction, solvent addition, and redispersion. Under these conditions, manual synthesis without SSP requires ≈115 min per batch, corresponding to a throughput of ≈4 batches per day. Incorporation of SSP increases the total processing time to ≈175 min per batch, thereby reducing the throughput to ≈2 batches per day. In contrast, automated workflow routinely achieves a throughput of 8 batches per day, with the present limitation arising from the number of available reactors.

Degree of automation: The degree of automation is defined as the number of synthesis steps implemented automatically within the workflow. In this study, five key steps are considered: reagent addition, temperature control, sampling, purification, and data logging. In the manual workflow, only temperature control is programmable; therefore, the degree of automation is assigned as 1 step. The automated workflow implements automated reagent addition, temperature control, sampling, and data logging, whereas purification remain manual; therefore, the degree of automation is assigned as 4 steps.

Purification yield: The purification yield (wt.%) in this work is defined as the mass fraction of CQDs retained after a given purification workflow, normalized to the total mass of CQDs in reaction product. For both automated and manual synthesis workflows without SSP, the crude reaction product is first centrifuged without adding antisolvent to remove the insoluble by-products. The supernatant then undergoes a single antisolvent-induced precipitation/redispersion cycle to remove excess ligands. This procedure results in a relative purification yield of ≈80%, with the remaining ≈20% lost due to CQDs discarded as supernatant in the last centrifugation.

When SSP is performed, the supernatant obtained after the initial purification step is further fractionated through five sequential precipitation/redispersion cycles.[21] Five size fractions (S1–S5) are obtained

with relative mass distributions of ≈30%, ≈30%, ≈20%, ≈10%, and ≈10%, respectively, normalized to the mass of CQDs retained after the single-precipitation step. The S5 fraction is typically selected as the final product due to its superior size uniformity, corresponding to an effective purification yield of 10% × 80% = 8% with respect to the total mass of CQDs in the reaction product.

Materials characterization

CQD samples were transferred into sealed quartz cuvettes with 1 mm path length for optical measurements. The optical absorption spectra were obtained using a QualitySpec Pro Vis/NIR Spectrometer. Steady-state PL spectra of InSb CQDs were obtained using the Horiba Fluorolog Spectrofluorometer using an excitation wavelength of 950 nm. Time-resolved PL measurements were performed using a time-correlated single photon counting (TCSPC) detector and a pulsed NIR laser diode (820 nm, Horiba).

TEM images were acquired using a Hitachi HT7700 TEM. HAADF-STEM images were acquired using the 200 kV cold field emission single spherical aberration-corrected electron microscope JEM-ARM200F NEOARM.

XRD measurements were performed using a Rigaku MiniFlex 600 powder X-ray diffractometer with monochromatized Cu K_α radiation. XPS was measured using a Thermo Fisher Scientific Escalab 250Xi system equipped with an Al K_α X-ray source (1486.6 eV).

Transmission SAXS measurements were collected from CQD samples dispersed in toluene or xylene (10–15 mg mL^{-1}) in sealed 1.5 mm capillary tubes using a SAXSLAB Ganesha instrument with a DECTRIS PILATUS3 R 300 K image plate detector (487 × 619 pixels, 0.172 × 0.172 mm^2 per pixel) and Cu K_α radiation (λ = 0.154 nm). The SAXS data were background subtracted using the corresponding solvent as blank.[36,37] Background corrected data were fitted with a spherical form factor in MATLAB.[38,39] The average radius and size polydispersity were extracted from the fits, where the size polydispersity is defined as the standard deviation of the fitted radius distribution divided by the mean radius.

Quantification of precursor reduction kinetics

Single-precursor reduction experiments were carried out by adding the reducing agent separately to $InCl_3$/OLAM or $SbCl_3$/OLAM precursor solutions. Precursor reduction was accompanied by progressive darkening of the reaction solution, which was recorded by video. The extent of solution darkening was quantified from video recordings using custom Python scripts implemented in OpenCV, NumPy and Pandas. For each experiment, a fixed rectangular region of interest (ROI) corresponding to the liquid phase was manually defined from the first frame and retained throughout analysis. Video metadata, including frame rate and frame count, were extracted directly from the source file to map each analyzed frame to reaction time.

Frames were sampled at 0.3 s intervals. The ROI of each sampled frame was converted to 8-bit grayscale and smoothed using a 5 × 5 Gaussian filter. Mean grayscale intensity, dark-pixel fraction (gray value < 65), and grayscale standard deviation were then calculated. Darkness was defined as 1-(mean 8-bit grayscale)/255, so that higher values indicate a darker reaction solution. To suppress short-timescale fluctuations, time-series data were smoothed using a centered rolling mean with a window size of 9 frames.

Synthesis of InAs CQDs with varying In/As precursor ratios

InAs CQDs were synthesized by varying the In/As precursor ratio while keeping the other reaction parameters constant. In a typical procedure, $InCl_3$ and $ZnCl_2$ were loaded into a 250 mL three-neck flask containing OLAM (15 mL) under an inert atmosphere. The mixture was dried at 120 °C under vacuum for 1 h. After degassing, the reaction mixture was heated to 150 °C. At this temperature, tris(dimethylamino)arsine ($As[N(CH_3)_2]_3$, 0.6 mmol) was injected into the flask, immediately followed by the injection of the reducing agent (alane *N*,*N*-dimethylethylamine complex solution, 1.8 mmol). The reaction mixture was then heated from 150 °C to 250 °C over 15 min and held at 250 °C for 15 min. The reaction was quenched to room temperature by cooling under N_2. For the synthesis with In/As molar ratio of 1:1, 0.6 mmol of $InCl_3$ and 3 mmol of $ZnCl_2$ were used. When the In/As molar ratio is increased to 3:1, the amounts of both $InCl_3$ and $ZnCl_2$ were increased proportionally to 1.8 and 9 mmol, respectively, while the amount of the arsenic precursor was fixed at 0.6 mmol.

The crude CQD solution was purified by the addition of toluene and ethanol, followed by centrifugation at 6350× *g* for 5 min. The resulting precipitate was redispersed in toluene and centrifuged again without antisolvent to remove insoluble byproducts. The collected supernatant was then precipitated with ethanol again, and this step was repeated for two additional times. The final CQD product was dispersed in toluene for further characterization. The optical absorption spectra were obtained using a combination of two Ocean Optics detectors (QE Pro and Ocean NR).

FET device fabrication, measurement, and mobility analysis

Bottom-gate top contact FET substrates were fabricated on thermal SiO_2 (291 nm)/Si(p^{++}) wafers with UV lithography patterned Ag electrodes.[35] The 2-mercaptoethanol-exchanged InSb CQDs were then deposited onto the prepatterned substrates, followed by annealing at 90 °C for 1 h. FET device measurements were carried out using a semiconductor parameter analyzer. Transfer curves were collected at a constant drain–source voltage of V_{DS} = +30 V, while output curves were obtained by sweeping V_{DS} under different V_{GS} values. The source electrode was kept grounded during all measurements.

The field-effect mobility was extracted from the linear operating regime of the InSb CQD transistor. In this regime, the drain–source current depends linearly on gate bias, following Eq. (3):

$$I_{DS,lin} = \mu C_i \frac{W}{L}\left((V_{GS} - V_{th})V_{DS} - \frac{V_{DS}^2}{2}\right) \tag{3}$$

where V_{th} denotes the threshold voltage and C_i is the areal capacitance of the gate dielectric, defined $C_i = \frac{\epsilon_r \epsilon_0}{t}$. Using ϵ_{r,SiO_2} = 3.9 for SiO_2, C_i was calculated to be 11.9 nF cm^{-2}. Because the device exhibits p-type transport, the hole mobility was determined from the slope of the linear portion of the transfer curve, $m_{lin} \equiv \frac{dI_{DS}}{dV_{GS}}$, according to Eq. (4):

$$\mu = m_{lin}\frac{L}{W}\frac{1}{V_{DS}}\frac{1}{C_i} \tag{4}$$

With a channel width-to-length ratio (*W*/*L*) of 62450, the calculated hole mobility was 4×10^{-5} cm^2 V^{-1} s^{-1}.

Reporting summary

Further information on research design is available in the Nature Portfolio Reporting Summary linked to this article.

Data availability

The data that support the findings of this study are available from the corresponding authors upon request. Supplementary Movies of single-precursor reduction processes are available from Zenodo[40]. Unprocessed raw data are provided as Supplementary Data 1. Source data are provided with this paper.

Code availability

The code used in this work for quantification of precursor reduction kinetics is available from Zenodo[41] and from the corresponding authors upon request.

References

1. García de Arquer, F. P. et al. Semiconductor quantum dots: technological progress and future challenges. *Science* **373**, 640 (2021).
2. García De Arquer, F. P., Armin, A., Meredith, P. & Sargent, E. H. Solution-processed semiconductors for next-generation photodetectors. *Nat. Rev. Mater.* **2**, 1–16 (2017).
3. Houtepen, A. J. et al. Colloidal quantum dots for optoelectronics. *Nat. Rev. Methods Prim.* **5**, 42 (2025).
4. Tang, X., Ackerman, M. M., Chen, M. & Guyot-Sionnest, P. Dual-band infrared imaging using stacked colloidal quantum dot photodiodes. *Nat. Photonics* **13**, 277–282 (2019).
5. Liu, J. et al. A near-infrared colloidal quantum dot imager with monolithically integrated readout circuitry. *Nat. Electron.* **5**, 443–451 (2022).
6. Madelung, O., Rößler, U. K. & Schulz, M. *Group IV Elements, IV-IV and III-V Compounds. Part B: Electronic, Transport, Optical and Other Properties*. (Springer, 2002).
7. Liu, M. et al. Hybrid organic-inorganic inks flatten the energy landscape in colloidal quantum dot solids. *Nat. Mater.* **16**, 258–263 (2017).
8. Peng, L. et al. Suppressing colloidal quantum dot multimer fusion leads to high-performance InSb infrared photodetectors. *Adv. Sci.* **12**, 2502775 (2025).
9. Liu, W., Chang, A. Y., Schaller, R. D. & Talapin, D. V. Colloidal InSb nanocrystals. *J. Am. Chem. Soc.* **134**, 20258–20261 (2012).
10. Zhao, T. et al. General synthetic route to high-quality colloidal III-V semiconductor quantum dots based on pnictogen chlorides. *J. Am. Chem. Soc.* **141**, 15145–15152 (2019).
11. Wang, Q. et al. Stepwise crystallization synthetic strategy for monodisperse InSb colloidal quantum dots with mid-infrared absorption. *Angew. Chem. Int. Ed.* **64**, e202506387 (2025).
12. Lee, S., Zhitomirsky, D. & Grossman, J. C. Manipulating electronic energy disorder in colloidal quantum dot solids for enhanced charge carrier transport. *Adv. Funct. Mater.* **26**, 1554–1562 (2016).
13. De Mello Donega, C. et al. Luminescent colloidal InSb quantum dots from in situ generated single-source precursor. *ACS Nano* **14**, 13146–13160 (2020).
14. Muhammad. et al. Halide-driven synthetic control of InSb colloidal quantum dots enables short-wave infrared photodetectors. *Adv. Mater.* **35**, 2306147 (2023).
15. Tovstun, S. A. & Razumov, V. F. Theory of size-selective precipitation. *J. Nanopart. Res.* **19**, 8 (2016).
16. Chan, E. M. et al. Reproducible, high-throughput synthesis of colloidal nanocrystals for optimization in multidimensional parameter space. *Nano Lett.* **10**, 1874–1885 (2010).
17. Li, Z. et al. Robot-accelerated perovskite investigation and discovery. *Chem. Mater.* **32**, 5650–5663 (2020).
18. Kim, M. A., Ai, Q., Norquist, A. J., Schrier, J. & Chan, E. M. Active learning of ligands that enhance perovskite nanocrystal luminescence. *ACS Nano* **18**, 14514–14522 (2024).
19. Xu, J. et al. Autonomous multi-robot synthesis and optimization of metal halide perovskite nanocrystals. *Nat. Commun.* **16**, 7841 (2025).
20. Zhao, H. et al. A robotic platform for the synthesis of colloidal nanocrystals. *Nat. Synth.* **2**, 505–514 (2023).
21. Imran, M. et al. Control over metal-halide reactivity enables uniform growth of InSb colloidal quantum dots for enhanced swir light detection. *Adv. Mater.* **37**, 2420273 (2025).
22. Tamang, S., Lee, S., Choi, H. & Jeong, S. Tuning size and size distribution of colloidal InAs nanocrystals via continuous supply of prenucleation clusters on nanocrystal seeds. *Chem. Mater.* **28**, 8119–8122 (2016).
23. Vikram, A. et al. Mechanistic insights into size-focused growth of indium phosphide nanocrystals in the presence of trace water. *Chem. Mater.* **32**, 3577–3584 (2020).
24. Kwon, Y. et al. Synthesis of NIR/SWIR absorbing InSb nanocrystals using indium(I) halide and aminostibine precursors. *Adv. Funct. Mater.* **34**, 2403912 (2024).
25. Zhu, D. et al. $ZnCl_2$ mediated synthesis of InAs nanocrystals with aminoarsine. *J. Am. Chem. Soc.* **144**, 10515–10523 (2022).
26. Abe, S., Čapek, R. K., De Geyter, B. & Hens, Z. Tuning the post-focused size of colloidal nanocrystals by the reaction rate: from theory to application. *ACS Nano* **6**, 42–53 (2012).
27. Leemans, J. et al. Formation of colloidal In(As,P) quantum dots active in the short-wave infrared, promoting growth through temperature ramps. *ACS Nano* **17**, 20002–20012 (2023).
28. Allan, G. & Delerue, C. Confinement effects in PbSe quantum wells and nanocrystals. *Phys. Rev. B* **70**, 245321 (2004).
29. Peng, L. et al. Synthesis of monodisperse InSb colloidal quantum dots by monomer concentration control for short-wave infrared photodetectors. *Nat. Commun.* **17**, 3871 (2026).
30. Yarema, M. & Kovalenko, M. V. Colloidal synthesis of InSb nanocrystals with controlled polymorphism using indium and antimony amides. *Chem. Mater.* **25**, 1788–1792 (2013).
31. Kim, M. et al. Surface-originated weak confinement in tetrahedral indium arsenide quantum dots. *J. Am. Chem. Soc.* **146**, 10251–10256 (2024).
32. Ko, J. H., Yoo, D. & Kim, Y. H. Atomic models for anionic ligand passivation of cation-rich surfaces of IV-VI, II-VI, and III-V colloidal quantum dots. *Chem. Commun.* **53**, 388–391 (2017).
33. Kim, T. et al. Development of group III-V colloidal quantum dots for optoelectronic applications. *ACS Energy Lett.* **8**, 447–456 (2023).
34. Zhang, Y. et al. Dicarboxylic acid-assisted surface oxide removal and passivation of indium antimonide colloidal quantum dots for short-wave infrared photodetectors. *Angew. Chem. Int. Ed.* **63**, e202316733 (2024).
35. Zhang, Y. et al. Nucleophilic covalent ligands enable simultaneous surface reconstruction and passivation of colloidal InSb quantum dots for stable short-wave infrared photodetectors. *Angew. Chem. Int. Ed.* **64**, e202505179 (2025).
36. Maes, J. et al. Size and concentration determination of colloidal nanocrystals by small-angle X-ray scattering. *Chem. Mater.* **30**, 3952–3962 (2018).
37. Sharma, A. A practical guide to acquisition, treatment and model-free analysis of SAXS/SANS data: methodologies and pitfalls. *Soft Matter* **22**, 2088–2106 (2026).
38. Korgel, B. A., Fullam, S., Connolly, S. & Fitzmaurice, D. Assembly and self-organization of silver nanocrystal superlattices: ordered "soft spheres. *J. Phys. Chem. B* **102**, 8379–8388 (1998).
39. Noh, J. et al. Colloidal germanium quantum dots with broadly tunable size and light emission. *J. Am. Chem. Soc.* **147**, 1792–1802 (2025).
40. Zhang, Y. & Bai, Y. Supplementary movies for Automated synthesis of InSb quantum dots with improved batch-to-batch reproducibility via kinetically matched co-reduction. *Zenodo*, https://doi.org/10.5281/zenodo.19956412 (2026).
41. Zhang, Y. & Bai, Y. Code for: Automated synthesis of InSb quantum dots with improved batch-to-batch reproducibility via kinetically matched co-reduction. *Zenodo*. https://doi.org/10.5281/zenodo.19958176 (2026).

Acknowledgements

The automated experimentation work was performed at the Molecular Foundry and was supported by the Office of Science, Office of Basic Energy Sciences, of the U.S. Department of Energy under Contract No. DE-AC02-05CH11231, under user proposal number MFP-8636. XPS measurements were performed at the University of Toronto's Open Center for the Characterization of Advanced Materials (OCCAM).

Author contributions

E.H.S. and E.C. supervised the project. Y.Z. conceived the project. Y.Z. and E.C. designed the experiments. Y.Z., H.W.B., and P.X. performed automated synthesis, purification, and optical characterization at the Molecular Foundry. Y.Z., H.W.B., P.X., and Y.B. analyzed optical data. S.H. performed FET measurements and analyzed the data. F.D. contributed to XPS sample preparation and measurements. C.L. analyzed HAADF-STEM data. Y.L. analyzed the reduction kinetics data under the guidance of Y.B. Y.Z. and E.N. performed TEM measurements. S.S. collected and analyzed SAXS data under the guidance of B.A.K. M.I., and S.H. provided suggestions on data analysis. Y.Z. and B.R. performed PL measurements. L.Z. assisted with XRD measurements. X.Q. assisted with automated experimentation. Y.Z., H.W.B., and P.X. wrote the paper. E.H.S. and E.C. edited the paper. All authors discussed and commented on the paper.

Funding

This work received financial support from the Natural Sciences and Engineering Research Council of Canada (NSERC) Alliance grant (ALLRP 590340-23). Y.B. received funding provided to the University of Toronto's Acceleration Consortium from the Canada First Research Excellence Fund (CFREF-2022-00042). B.A.K. and S.S. received funding by Robert A. Welch Foundation (F-1464) and the Center for a Solar Powered Future—a National Science Foundation Industry University Cooperative Research Center (IUCRC) (EEC-2052814).

Competing interests

The authors declare no competing interests.

Additional information

Supplementary information The online version contains supplementary material available at https://doi.org/10.1038/s41467-026-74136-3.

Correspondence and requests for materials should be addressed to Emory Chan or Edward H. Sargent.

Peer review information *Nature Communications* thanks Igor Fedin, and the other, anonymous, reviewers for their contribution to the peer review of this work. A peer review file is available.